

Competing magnetic states in transition metal dichalcogenide moiré materials

Nai Chao Hu¹ and Allan H. MacDonald¹

¹*Department of Physics, The University of Texas at Austin, Austin, TX 78712, USA.*

(Dated: December 3, 2021)

Small-twist-angle transition metal dichalcogenide (TMD) heterobilayers develop isolated flat moiré bands that are approximately described by triangular lattice generalized Hubbard models [1]. In this article we explore the metallic and insulating states that appear under different control conditions at a density of one-electron per moiré period, and the transitions between them. By combining fully self-consistent Hartree-Fock theory calculations with strong-coupling expansions around the atomic limit, we identify four different magnetic states and one nonmagnetic state near the model phase diagram’s metal-insulator phase-transition line. Ferromagnetic insulating states, stabilized by non-local direct exchange interactions, are surprisingly prominent.

I. INTRODUCTION

Moiré materials, formed by stacking layered 2-dimensional (2D) van der Waals semiconductors or semimetals with small differences in lattice constant or orientation, have attracted attention recently as a highly tunable platform to study strong correlation phenomena. The low energy physics of a moiré material is accurately described by an emergent periodic Hamiltonian [1–3] that is insensitive to commensurability between the moiré pattern and the underlying lattice. Stimulated by the recent experimental realization [4–6] of magic angle physics in twisted bilayer graphene, experimental attention has expanded to include other graphene based multilayers with twists [7–14], and also twisted transition metal dichalcogenide bilayers [15–25]. The valence bands of TMD heterobilayers and Γ -valley homobilayers [26] are described by emergent models in which interacting spin-1/2 electrons experience an external potential with triangular lattice periodicity, and therefore map directly to models of electrons on triangular or honeycomb lattices. This paper is devoted to a study of the properties of triangular lattice moiré materials and focuses on the case of one-hole per moiré period, where correlations are strongest. We examine the crossover from the narrow-band regime at small twist angles, where the system maps to a one-band Hubbard model with dominant on-site interactions, to the regime closer to the metal-insulator phase transition where important differences appear.

Our discussion is based mainly on a mean-field Hartree-Fock approximation used to address the interplay between periodic modulation and Coulomb interactions that controls the hybridization between orbitals centered on different sites, and therefore exchange interactions of spins on the system’s triangular lattice. Because it is a mean-field approach, the Hartree-Fock approximation cannot account for dynamic fluctuations in spin-configuration, but can accurately describe the energy of particular spin-configurations. Importantly for the present application, the Hartree-Fock approximation has the advantage over spin-density-functional theory [27] that it correctly accounts for the absence of self-interaction [28] when electrons are localized near lat-

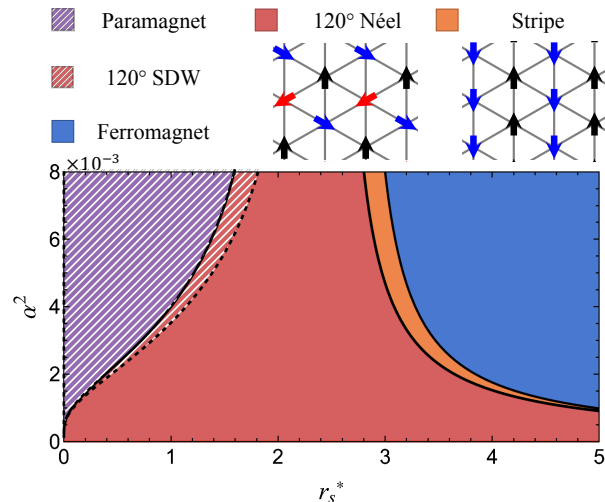


FIG. 1. Hartree-Fock phase diagram for triangular lattice moiré materials with one hole per unit cell. The two dimensionless control parameters (see main text) are the interaction strength r_s^* and α^2 - a parameter that is inversely related to the moiré potential strength. First order and second order phase transitions are marked by solid and dashed black lines, respectively. States close to the top-left corner of the phase diagram (hashed) are metallic. States at the bottom right of the phase diagram are insulating. A narrow semi-metallic state (labelled SDW - spin density wave) that shares spatial symmetries with the three-sublattice non-collinear insulating state hugs the metallic side of the metal-insulator transition. An unexpected phase transition into an insulating ferromagnetic (blue) state at strong interaction strengths is interrupted by a narrow collinear antiferromagnetic stripe state (orange). This phase diagram was calculated for moiré modulation phase (see main text) $\phi = 26^\circ$. The lines in this figure follow approximate phase boundary expressions explained in the main text.

tice sites. We expect the Hartree-Fock approximation to overestimate the stability of insulating states relative to metallic states. (Indeed this expectation is confirmed by comparison with separate exact-diagonalization calculations for the same model [29].) Our calculations can therefore provide a lower bound on the moiré modulation strength that drives the system from a metallic to

an insulating state at a given interaction strength. Unlike exact-diagonalization calculations, Hartree-Fock calculations can be accurately converged with respect to system size.

Our goal in this manuscript is to identify differences between moiré material physics and single-band Hubbard model physics, with particular emphasis on the prospects for tuning the system into exotic spin liquid states. Fig. 1 shows the phase diagram in a space defined by dimensionless modulation strength $\alpha^2(V_M, \phi, a_M)$ and interaction strength $r_s^*(\epsilon, a_M)$ parameters. The full phase space of the problem is actually 3-dimensional since the phase (ϕ - see below) of moiré potential Fourier amplitude also plays a role. (a_M is the moiré material lattice constant.) The lowest energy hole band is spectrally isolated for $\alpha \lesssim 0.1$, the range covered in Fig. 1, unless ϕ is very close to a honeycomb value. (See below.) We find that the three sublattice antiferromagnetism expected [30] in the insulating state transform to stripe magnetism and finally to ferromagnetism with increasing r_s^* , and that a semimetallic state with three sublattice order occurs on the metallic side of the metal-insulator phase transition. The transition to ferromagnetic insulating states at strong interactions opens up new opportunities to engineer strongly frustrated quantum magnetism. Given the possibility of *in situ* tuning between different spin states, these findings demonstrate that moiré materials are an exceptionally promising new system for the exploration of two-dimensional quantum magnetism.

The rest of the paper is organized as follows: In Sec. II we review the moiré material model, discuss expected properties, and introduce the mean-field formalism. In Sec. III, we discuss our results for spin-interactions in insulating moiré materials. We comment specifically on necessary conditions for non-zero Hall conductance, concluding that though non-trivial band topology is unlikely, applying a magnetic field might induce a non-zero Hall conductance in doped insulators. Finally in Sec. IV we summarize our results and highlight important directions for future research.

II. INTERACTING CONTINUUM MODEL

The low energy physics of TMD moiré materials, like that of twisted bilayer graphene, is most conveniently captured by a continuum model [1]. Since TMDs are generally good insulators with strong spin-orbit coupling from the transition metal atoms, only the topmost valence band needs to be included in the low energy model - yielding one state for each valley. Because of spin-valley locking, we can equivalently choose to identify these states by their spins or by their valleys. The type-II band alignment of TMD heterojunctions means that only one layer is active at low energy. Hence the fermion field operators $\psi_\alpha^{(\dagger)}(\mathbf{r})$ in this model carry only one label, representing locked spin/valley, while the effect of the other layer is integrated out, appearing only as

a contribution to the moiré potential [1, 31], $\Delta(\mathbf{r})$. When the Fourier expansion of Δ is truncated at the first shell of moiré reciprocal lattice vectors \mathbf{b}_j ,

$$\Delta(\mathbf{r}) = \sum_{j=1}^6 V_j \exp [i\mathbf{b}_j \cdot \mathbf{r}], \quad (1)$$

where $V_j = V_M \exp [(-1)^{j-1} i\phi]$. V_j and ϕ are material-dependent parameters, with V_M characterizing the moiré modulation strength and ϕ its shape. The single-particle Hamiltonian of the moiré continuum model

$$H_0 = T + \Delta(\mathbf{r}), \quad (2)$$

where T is the single-particle kinetic energy operator for electrons with effective mass m^* , is spin-independent. In a plane-wave representation

$$H_{0\mathbf{b},\mathbf{b}'}(\mathbf{k}) = -\frac{\hbar^2}{2m^*} (\mathbf{k} + \mathbf{b})^2 \delta_{\mathbf{b},\mathbf{b}'} + \sum_{j=1}^6 V_j \delta_{\mathbf{b}_j, \mathbf{b}-\mathbf{b}'}, \quad (3)$$

where momentum \mathbf{k} is in the first moiré Brillouin zone and the \mathbf{b} 's are moiré reciprocal lattice vectors.

The key feature of this single-particle model, as pointed out in Ref. [1], is that the lowest energy hole band is isolated and has a bandwidth W that decreases exponentially with moiré period a_M . One physical intuition for this behavior is based on the observation that the model can be approximated, in the large- a_M limit, as a lattice of weakly coupled harmonically confined electrons. Ignoring the “remote-band” holes for the moment, we can readily see that the largest effect of Coulomb interactions is to impose an energy penalty U on doubly occupied sites, which is the essence of Hubbard model physics. But in contrast to simplest nearest-neighbor Hubbard model, the ratio of second nearest-neighbor hopping to the nearest-neighbor hopping can be increased by decreasing the modulation strength, a property easily explained in the harmonic oscillator approximation, increasing the magnetic frustration of insulating states.

In addition to allowing flexible tuning of U/W , the sublattice content of the hexagonal Bravais lattice on which the model sits can be controlled. The symmetry of the moiré potential can be changed from that of a triangular lattice to that of a honeycomb lattice, with perfect honeycomb behavior achieved at $\phi = 60^\circ$, $\phi = 180^\circ$ and $\phi = -60^\circ$. The applicable value of ϕ can be adjusted experimentally by choosing different TMD heterojunctions [27, 29]. Over a finite range of ϕ near the honeycomb values, the moiré potential has local minima at the honeycomb lattice sites. When ϕ is close to one of the honeycomb values, the potential minima at the two honeycomb sublattices differ slightly in value, allowing inversion-symmetry breaking sublattice-mass terms to be added to the Hamiltonian when expressed in terms of its tight-binding model limit. Here we focus on triangular lattice Hubbard model Mott physics by restricting our attention to the case of one electron per triangular lattice

unit cell. At this density the second minimum plays a role only over narrow ranges of ϕ by increasing the spread of ground state Wannier wave function and slightly altering the competition between different states.

The many-body Hamiltonian in TMD moiré materials has three terms: the kinetic energy, the moiré modulation potential, and the Coulomb interaction term. It follows that the many-body physics depends, up to an energy scale, on ϕ and on two dimensionless parameters. We choose to describe the phase diagram in terms of the standard electron gas interaction strength parameter,

$$r_s^* = \frac{1}{\sqrt{\pi n a_B^*}} = \left(\frac{3}{4\pi^2}\right)^{1/4} \frac{V_C^s}{T^s} = \left(\frac{3}{4\pi^2}\right)^{1/4} \frac{a_M}{a_B} \frac{m^*}{m} \frac{1}{\epsilon}, \quad (4)$$

and a second parameter that characterizes the ratio of the single-particle Wannier function spread to the moiré period. Here we have defined two energy scales: the kinetic energy scale at the moiré length $T^s = \hbar^2/2m^*a_M^2$ and the Coulomb interaction at the moiré length $V_C^s = e^2/2\epsilon a_M$, and one length scale - the Bohr radius $a_B^* \equiv \hbar^2\epsilon/e^2m^*$. Our interaction strength parameter r_s^* can be viewed as the typical distance between electrons in Bohr radius units. The definition of the second dimensionless parameter is motivated by the small twist angle limit in which the lowest energy flat-band's Wannier function is accurately approximated by the Gaussian ground state of the harmonic potential $m^*\omega^2\mathbf{r}^2/2$ obtained by expanding the moiré modulation potential around a minimum. It follows from this expansion that $\omega^2 = \beta V_M/m^*a_M^2$ where $\beta = 16\pi^2 \cos(\phi + k120^\circ)$, with k an integer chosen to place the argument of the cos-function $\in (-60^\circ, 60^\circ)$ [32]. We choose

$$\alpha \equiv \frac{a_W^2}{a_M^2} = \frac{\hbar}{\sqrt{m^*\beta V_M a_M^2}}, \quad (5)$$

where $a_W^2 = \hbar/m^*\omega$ is the square of the oscillator length scale, as the second dimensionless interaction parameter. Notice that α is dependent on both the phase ϕ and the magnitude V_M of the moiré potential. In Fig. 1 the phase diagram is plotted in terms of r_s^* and α^2 , with the latter variable chosen to simplify its dependence on V_M . Choosing α as a dimensionless model parameter eliminates most of the phase diagram's dependence on ϕ , with exceptions applying very close to $\phi \sim 60^\circ + k120^\circ$, and deep in the metallic state.

A. Symmetries

For later convenience, we briefly summarize the symmetries of the problem. The model has a full SU(2) rotation symmetry of the locked spin/valley degree-of-freedom and C_{3v} orbital symmetry; the D_{3h} symmetry of a TMD monolayer is reduced by stacking. The non-trivial operations of C_{3v} are rotation by $2\pi/3$,

$$C_3 : \psi_\alpha(\mathbf{x}) \rightarrow \psi_\alpha(R_{2\pi/3}\mathbf{x}), \quad (6)$$

and the mirror operation M_y ,

$$M_y : \psi_\alpha(x, y) \rightarrow \psi_\alpha(x, -y). \quad (7)$$

In the absence of a magnetic field, the model is invariant under time reversal, which switches the spins:

$$\mathcal{T} : \psi_\alpha(\mathbf{x}) \rightarrow i(\sigma^y)_{\alpha\beta} \psi_\beta(\mathbf{x}), \quad (8)$$

where σ^y is the Pauli matrix acts in the spin space. We note that two spins are only interchanged by time reversal symmetry (TRS):

$$H_{\mathbf{b},\mathbf{b}'}^\downarrow(\mathbf{k}) = H_{-\mathbf{b},-\mathbf{b}'}^{\uparrow*}(-\mathbf{k}), \quad (9)$$

where we make use again of the discrete translational invariance of our moiré system. At this level of approximation, each spin projected Hamiltonian itself also satisfies a spinless TRS property:

$$H_{\mathbf{b},\mathbf{b}'}^{\uparrow/\downarrow}(\mathbf{k}) = H_{-\mathbf{b},-\mathbf{b}'}^{\uparrow/\downarrow}(-\mathbf{k}). \quad (10)$$

We also note that since inversion symmetry is broken in TMD monolayers, unlike in twisted bilayer graphene, Berry curvature is not required to vanish identically throughout the moiré Brillouin zone.

B. Weak and Strong Modulation Limits

Before carrying out detailed self-consistent Hartree-Fock calculations, we provide some orientation by discussing some simple limits in which electronic properties are well understood. We first consider the weak modulation limit, where bandwidths are large and moiré bands overlap, which should give rise to behavior close to that of the 2D homogeneous electron gas (jellium) model. It is well known that Hartree-Fock approximation fails badly for magnetic properties by predicting that 2D jellium is ferromagnetic above a small value of $r_s \simeq 2.01$, whereas quantum Monte Carlo calculations [33, 34] shows that the paramagnetic fluid remains stable up to a much larger interaction strength $r_s \sim 25.56$. In the opposite strong modulation limit electrons occupy Wannier functions centered on potential minima. At one electron per moiré period, strong on-site Coulomb interactions leave only spin-degrees of freedom at low energies. Because electronic correlations are less subtle in this limit, Hartree-Fock approximation predicts magnetic states much more reliably, and we can fit ground state energies to determine the parameters of spin Hamiltonians. The only quadratic spin Hamiltonian that satisfies all the symmetry requirement of our model is the isotropic Heisenberg model:

$$H_{spin} = J_1 \sum_{\langle i,j \rangle} \mathbf{S}_i \cdot \mathbf{S}_j + J_2 \sum_{\langle\langle i,j \rangle\rangle} \mathbf{S}_i \cdot \mathbf{S}_j, \quad (11)$$

where $\langle i, j \rangle$ and $\langle\langle i, j \rangle\rangle$ label nearest-neighbor and next-nearest-neighbor interactions. In the case of $J_1 > 0$,

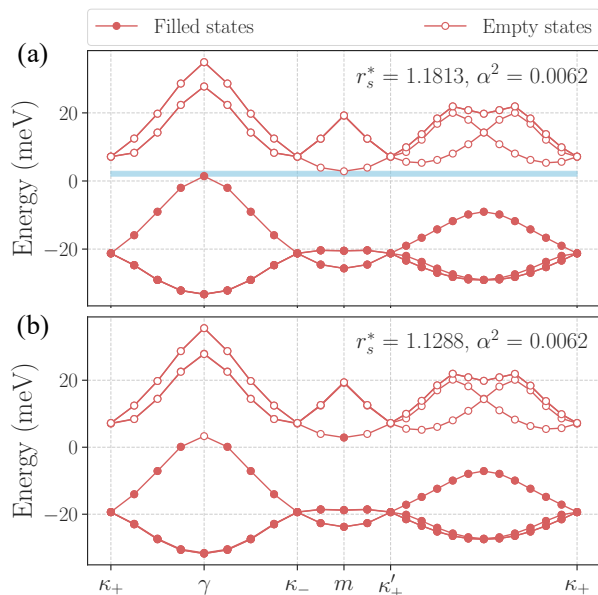


FIG. 2. Typical Hartree-Fock band structures for three-sublattice magnetic states: (a) 120° Néel insulator. The energy gap, indicated by the light-blue band, is small because the state is close to near the metal-insulator phase transition. At smaller r_s^* , we obtain (b) a 120° semimetallic SDW state. (See Appendix. A for further detail on model parameters.)

the classical-spin triangular-lattice ground state is the 120° Néel state for $J_2/J_1 < 1/8$ and a stripe state for $1/8 < J_2/J_1 < 1$ [30]. It's widely believed that quantum fluctuations play a vital role in determining the phase near $J_2/J_1 = 1/8$, although extensive numerical efforts over the years [35–40] have not reached a clear consensus on the nature of the potentially exotic phase. When the strong modulation Hamiltonian is approximated by a Hubbard model both interactions are antiferromagnetic [41]. with $J_2/J_1 \ll 1$, except possibly very close to the metal-insulator phase transition. In the present system, however, we find that insulating states are ferromagnetic at large r_s^* and interpret this property as evidence for beyond Hubbard-model physics. The band topology of the ferromagnetic state obviously has zero Chern number since spin-projected bands are then time-reversal invari-

ant. The topology of the 120° Néel is less obvious since \uparrow and \downarrow band states are mixed by the non-collinear spin structure. We nevertheless find that they are topologically trivial, as we show in Sec. III. For extremely localized electrons ($\alpha \rightarrow 0$), all magnetic configurations will become degenerate.

C. Self-consistent Hartree-Fock approximation

Our main goals in this MS are to gain insight into the spin-physics of the moiré superlattice Mott insulator phase, and to obtain a rough estimate of the boundary between insulating and metallic states. As long as the spin-ground state is close to its classical limit, that is to say as long as fluctuations in spin-direction in the magnetic ground state are not extremely large, the Hartree-Fock approximation is normally accurate. One important advantage of the Hartree-Fock approximation is that it completely removes spurious self-interaction effects in the limit that the electrons are reasonably strongly localized around their moiré lattice sites. As the twist angle is increased and the moiré pattern's lattice constant is reduced, two-dimensional spin-density functional theory [27], which has much the same structure as Hartree-Fock theory, becomes an attractive alternative. Even when quantum spin-fluctuations in the insulating ground state are large, either approach can be used to approximate the classical energy function of the spin subsystem, and quantum corrections can be calculated using standard spin-wave techniques.

The Hartree-Fock energy functional is the expectation value of the many-electron Hamiltonian in a single Slater determinant ground state. Minimizing the energy functional with respect to single-particle wave-functions yields a mean-field Hamiltonian that adds an interaction self-energy Σ^{HF} to the single-particle Hamiltonian which can be expressed in terms of the single-particle density matrix $\rho = \sum_n |\psi_n\rangle \langle \psi_n|$, where the sum is over occupied moiré-band Bloch wavefunctions. The mean-field electronic structure of moiré superlattices is best evaluated using a plane-wave representation in which the Hartree-Fock self energy Σ^{HF} at each \mathbf{k} in the Brillouin-zone is a matrix in reciprocal lattice vectors \mathbf{b} :

$$\Sigma_{\alpha,\mathbf{b};\beta,\mathbf{b}'}^{HF}(\mathbf{k}) = \frac{\delta_{\alpha,\beta}}{A} \sum_{\alpha'} V_{\alpha'\alpha}(\mathbf{b}' - \mathbf{b}) \sum_{\mathbf{k}',\mathbf{b}''} \rho_{\alpha',\mathbf{b}+\mathbf{b}'';\alpha',\mathbf{b}'+\mathbf{b}''}(\mathbf{k}') - \frac{1}{A} \sum_{\mathbf{b}'',\mathbf{k}'} V_{\alpha\beta}(\mathbf{b}' + \mathbf{k}' - \mathbf{k}) \rho_{\alpha,\mathbf{b}+\mathbf{b}'';\beta,\mathbf{b}'+\mathbf{b}''}(\mathbf{k}'). \quad (12)$$

In Eq. 12 Greek letters label spin, A is the finite sample area corresponding to a discrete Brillouin-zone mesh, and $\rho_{\alpha,\mathbf{b};\beta,\mathbf{b}'}$ is the self-consistently determined momentum-space density matrix. Starting with a physically plausible density matrix ρ_0 , we minimize the energy by performing self-consistent iterations. Because the many-body in-

teraction is invariant under both translations and spin-rotations, if we start from a density matrix ρ_0 which satisfies a symmetry \hat{O} of H_0 ($[\rho_0, \hat{O}] = 0$, $[H_0, \hat{O}] = 0$) then the symmetry survives under iteration. That is to say that H^{HF} commutes with \hat{O} at every iteration step. In many-cases the minimum energy Hartree-Fock state

breaks symmetries of H_0 and these solutions are found under iteration only by starting with a broken-symmetry density-matrix. As argued in Sec. II B, the phase diagram contains paramagnetic states that do not break any symmetries, ferromagnetic states with spontaneous collinear spin-polarization that do not break lattice translational symmetries, stripe states with collinear order and a doubled unit cell area, and 120° Néel states with both a tripled unit cell area and non-collinear spin-order. We obtain solutions of the first two kinds by appropriate choices of the initial density ρ_0 . Each possible type of reduced translational symmetry implies a different reciprocal lattice, and therefore has to be encoded explicitly in the reciprocal lattice employed and considered separately. Solutions can be classified as insulating with a gap between occupied and empty states, or metallic with Fermi surfaces in the Brillouin-zone on which occupation numbers change. At one electron per moiré period, the paramagnetic state must be metallic, but all other states we consider can be insulating. We show typical Hartree-Fock self-consistent band structures for insulating and metallic magnetic ordered states in Fig. 2.

III. RESULTS

Having introduced the problem we now present the predictions of Hartree-Fock theory for the phase diagram. We focus first on a fixed moiré modulation phase $\phi = 26^\circ$, estimated [1] to apply to the $\text{WSe}_2/\text{MoSe}_2$ heterobilayer system. (As emphasized earlier we have chosen the dimensionless parameters used to construct the phase diagrams with a view toward minimizing any dependence on ϕ .) We have performed self-consistent Hartree-Fock calculations on a discrete two-dimensional grid of system parameters. The phase diagram in Fig. 1 was constructed by interpolating between this discrete set of results; a pixelated summary of our actual calculation results is presented in Fig. 7 of the supplementary material. The influence of ϕ on the phase diagram will be discussed later.

Each solution of the Hartree-Fock equations corresponds either to a local minimum of the energy functional, or to a saddle point at which energy can be reduced by breaking symmetries. We have identified the ground state by comparing the total energies of all solutions. Translational symmetry is allowed to break down only to either the two sublattice (stripe) state or the three-sublattice (120°) state, both of which are common in triangular lattice phase diagrams. In our calculations, all phase transitions that change translational symmetry are of the first order, and all that do not are continuous.

Two sets of two phase boundaries are of particular interest: metal-insulator transitions on the left-hand side of Fig. 1 and magnetic transitions within the insulating state on the right-hand side. We see in Fig. 1 that the competition near the metal-insulator phase transition is mostly between a non-magnetic metallic state and

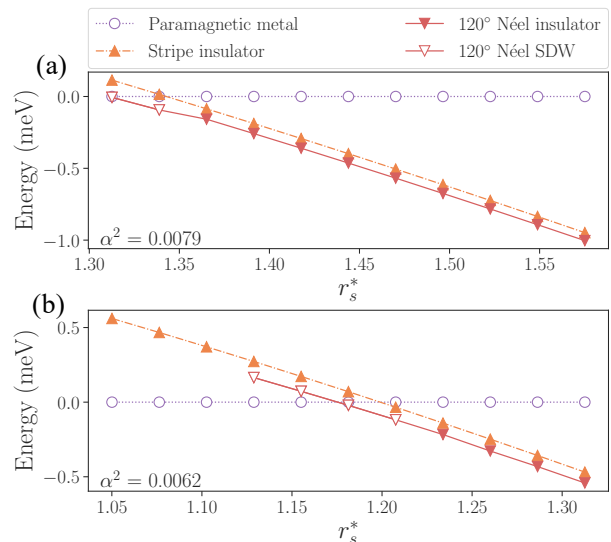


FIG. 3. We choose two values of the Wannier localization parameter α^2 to closely examine the emergence of the 120° semimetallic SDW state and the disappearance of metallic states with increasing r_s^* . Energies are plotted relative to the nonmagnetic metallic state energy. The ferromagnetic state has higher energy than both antiferromagnetic structures and is hence omitted in these plots. At the relatively large α^2 values we choose, the lowest energy state clearly change from paramagnetic metal to a 120° semimetallic SDW, and then to a 120° antiferromagnetic insulator.

the noncollinear three-sublattice state. When we examine the region near the metal-insulator phase transition closely, however, we find that the three-sublattice insulator becomes a semimetal at a critical r_s^* that is slightly larger than the critical r_s^* at which the magnetic order disappears. (See Fig. 3.) As a result, itinerant magnets with the same magnetic structure as that of the non-collinear three-sublattice insulating state appears near the metal-insulator transition. Thus within the Hartree-Fock approximation, the insulator-to-metal transition is a continuous phase transition, but is closely followed by a first order transition to a non-magnetic metallic state. We associate the increasing stability of 120° semimetallic SDW states, relative to 120° insulating states at larger values of α with increased increasing itineracy and associated larger values of t_2/t_1 . We also find that close to the metal-insulator phase boundary, the stripe and 120° insulating states have very similar energy densities, although the stripe order energies are always slightly larger.

To gain some analytic insight into the form of this phase boundary, we make an approximation that is accurate in the small twist angle limit discussed earlier. We estimate the nearest neighbor hopping parameter by using harmonic oscillator wave functions which yields

$$t_1 = \frac{\hbar^2}{2m^*a_M^2} \left(\frac{1}{4\alpha^2} - \frac{1}{\alpha} \right) \exp\left(-\frac{1}{4\alpha}\right). \quad (13)$$

The non-monotonic dependence of t_1 on α is related to a

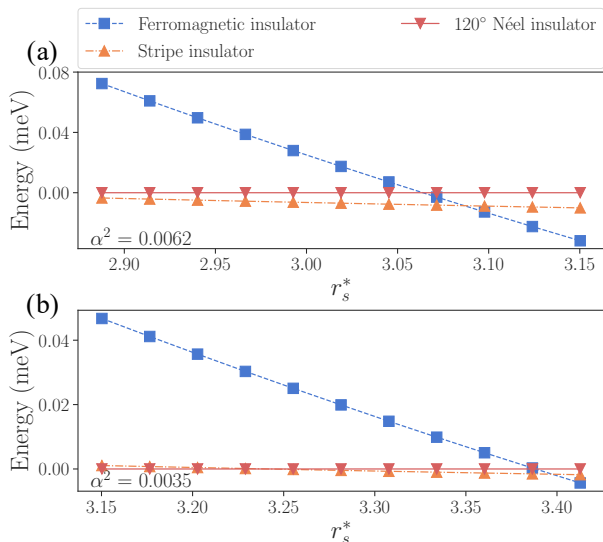


FIG. 4. Phase competition near the antiferromagnet-ferromagnet transition. Again the Wannier localization parameter α^2 is fixed and interaction strength r_s^* is varied. Energies are plotted relative to the 120° Néel insulators. Paramagnetic metals in this case have much higher energy than any insulators and therefore are omitted. The lowest energy state changes from a 120° antiferromagnetic insulator at small r_s^* to a stripe insulator, and then to a ferromagnetic insulator at large r_s^* . The stripe phase becomes more stable at larger α .

breakdown of the assumption of strongly localized Wannier orbitals at small α . To simplify the approximate phase boundary expression we derive below we measure energies in units of the moiré kinetic energy scale T^s and write $\tilde{X} \equiv X/T^s$. On physical grounds, the metal-insulator transition should occur at a critical value of the ratio $c = U/t_1$. Since the ratio of the moiré lattice constant to the Wannier function width, which is $\propto \theta^{1/2}$ changes slowly in the parameter range of interest, this criterion corresponds approximately to a critical c' of the ratio V_C^s/t_1 , which is proportional to r_s^* . (See Eq. (4).) In estimating the phase boundary line we ignore the $1/\alpha$ factor in Eq. (13) since α is small. This yields $\alpha^2 = [8W_{-1}(-\sqrt{t_1}/4)]^{-2}$, where $W_{-1}(x)$ is the Lambert W function and the branch is chosen by the monotonic property of t_1 . The Hartree-Fock metal-insulator phase boundary closely follows the $c' = 1.9$ line in the phase diagram, which corresponds to $c = 2c'/\sqrt{\alpha} \sim 15.1$. Given this value for c , we can estimate that the magnetic ordering energy on the insulating side of the phase diagram $4t_1^2/U$ is $\sim 4.0\text{meV}$ for experimental systems with moiré period $a_M \sim 5\text{nm}$ [23, 24], which compares well to the experimental estimate of $J_1 \sim 3\text{meV}$ [23].

We now turn to the magnetic transitions that occur within the insulating region in the phase diagram. We find that the insulators are ferromagnetic at large r_s^* , and that all magnetic states are very close in energy near the 120° state to ferromagnet phase boundary. Evidently this phase boundary is associated with a change in sign of

the dominant near-neighbor interactions between spins, leaving all states close in energy. The energies of competing states close to this phase boundary are plotted in Fig. 4, where we see that the ferromagnetic state is strongly favored at large interaction strength r_s^* , that stripe phase are stable over a narrow range of r_s^* between the 120° and ferromagnetic states, and that the stripe state stability range broadens at larger α .

To understand these observations, we consider interactions within the spin-only Hilbert space discussed in Sec. II B. Assuming the spin Hilbert space is correctly described by the $J_1 - J_2$ spin model of Eq. (11), the classical energies of the ferromagnetic, stripe, and 120° states are

$$e_1 = \frac{1}{4N}(3NJ_1 + 3NJ_2) = \frac{3}{4}J_1 + \frac{3}{4}J_2, \quad (14)$$

$$e_2 = \frac{1}{4N}(-NJ_1 - NJ_2) = -\frac{1}{4}J_1 - \frac{1}{4}J_2, \quad (15)$$

$$e_3 = \frac{1}{4N}(-3NJ_1/2 + 3NJ_2) = -\frac{3}{8}J_1 + \frac{3}{4}J_2. \quad (16)$$

It follows that can determine numerical values for the coupling constants from the energy differences between the three magnetic states we consider in our Hartree-Fock calculations:

$$J_1 = \frac{8}{9}(e_1 - e_3), \quad (17)$$

$$J_2 = e_1 - e_2 - J_1. \quad (18)$$

We plot the J_1 and J_2 values obtained in this way in Fig. 5, where we see that the signs of J_1 and J_2 are strongly correlated, and that the ferromagnetic state phase boundary aligns with the line on which J_1 changes sign.

One of the most intriguing aspects of our results is the appearance (at the mean field level) of a stripe state. This finding suggests that these moiré materials may provide a clean realization of the long-sought J_1 - J_2 quantum spin liquid state, which is born out of the quantum fluctuations near the boundary between the three-sublattice state and the stripe state. However, we caution the readers that our system is not fully equivalent to a J_1 - J_2 model. In the case of an exact J_1 - J_2 Heisenberg model, stripe states appear for $J_2/J_1 \gtrsim 1/8$. Since we estimate values of the exchange couplings by comparing energies of a small number of magnetic configurations, our results do not rule out other possibilities, one example of which is that the third nearest neighbour exchange coupling J_3 is ferromagnetic and $-J_3/J_1 \gtrsim 1/9$. Since current experimental studies operate in parameter ranges close to the metal-insulator transition, they may need to tune to larger r_s^* to reach the ferromagnetic state, for example by choosing materials with smaller lattice mismatches or tuning twist angles.

The J_1 sign change is associated with interactions that are non-local in the model's Wannier function lattice representation [42], and therefore absent in generalized Hubbard-model interaction approximations. For a

given pair of near-neighbor sites the non-local interaction terms can be characterized as either an interaction-assisted hopping term,

$$V_{ah} = \sum_{\sigma} \langle 2\sigma, 1\bar{\sigma} | V_C | 1\sigma, 1\bar{\sigma} \rangle c_{2\sigma}^{\dagger} c_{1\bar{\sigma}}^{\dagger} c_{1\bar{\sigma}} c_{1\sigma}, \quad (19)$$

or as a intersite-exchange term,

$$V_x = \sum_{\sigma_1, \sigma_2} \langle 2\sigma_1, 1\sigma_2 | V_C | 1\sigma_1, 2\sigma_2 \rangle c_{2\sigma_1}^{\dagger} c_{1\sigma_2}^{\dagger} c_{2\sigma_2} c_{1\sigma_1}, \quad (20)$$

where σ is a spin label and $\bar{\sigma} = -\sigma$. At half-filling, V_{ah} is physically equivalent to hopping, so its main effect is to enhance the antiferromagnetic coupling constant. On the other hand, V_x , being an exchange term, carries a minus sign from fermionic ordering and therefore favors ferromagnetic coupling [43]. We now argue the transition happens when the enhanced antiferromagnetic coupling $4(-t_1 + |V_{ah}|)^2/U$ is equal to $2|V_x|$ in magnitude. We assume we are in the strongly interacting regime where $V_{ah/x} \sim t_1^2/U \ll t_1$. This allows us to compare the simplified antiferromagnetic energy scale $4t_1^2/U$ to ferromagnetic energy scale

$$2|V_x(\mathbf{1}, \mathbf{2}; \mathbf{2}, \mathbf{1})| = 2U \exp\left(-\frac{1}{2\alpha}\right), \quad (21)$$

where $\mathbf{1}$ and $\mathbf{2}$ are nearest neighbors. We again ignore the $1/\alpha$ factor in the expression Eq. (13) of t_1 to the lowest order. It's clear then the antiferromagnet-ferromagnet phase boundary should be described by $1/2\sqrt{2}\alpha^2 = \tilde{U}$, i.e. $\alpha^2 = 1/2\sqrt{2}\tilde{U} \sim 1/r_s^*$ [44], which agrees well with our Hartree-Fock approximation.

To explicitly explore the influence of ϕ on the phase boundaries that remains for our choice of dimensionless interaction parameters, we carry out self-consistent Hartree-Fock calculations *vs.* ϕ at two points in our $r_s^* - \alpha^2$ phase diagram (Fig. 1) that lie just to the right of the two phase transition boundaries. In order to describe how the generic triangular lattice smoothly evolves into a honeycomb lattice we consider the range from $\phi = 30^\circ$ to $\phi = 60^\circ$ at which the additional honeycomb lattice symmetries become exact. Because we study the case of one-electron per-triangular lattice unit cell, the electron density is half of that associated with honeycomb lattice Mott insulator states. As ϕ approaches 60° , the two-local potential minima in the moiré unit cell become more nearly equivalent, and inversion symmetry relative to the mid-point between the two minima is more nearly established. In our self-consistent Hartree-Fock calculations we find that at the density we study this approximate symmetry is always strongly broken. Even at $\phi = 60^\circ$, the electrons tend to occupy one honeycomb sublattice only, as we verify by explicit calculation, and the role of the difference between ϕ and 60° acts as a weak symmetry-breaking parameter. At no point in this evolution do the lowest two self-consistent Hartree-Fock bands overlap and develop the Dirac points of single-orbital honeycomb lattice bands. The broken symmetry

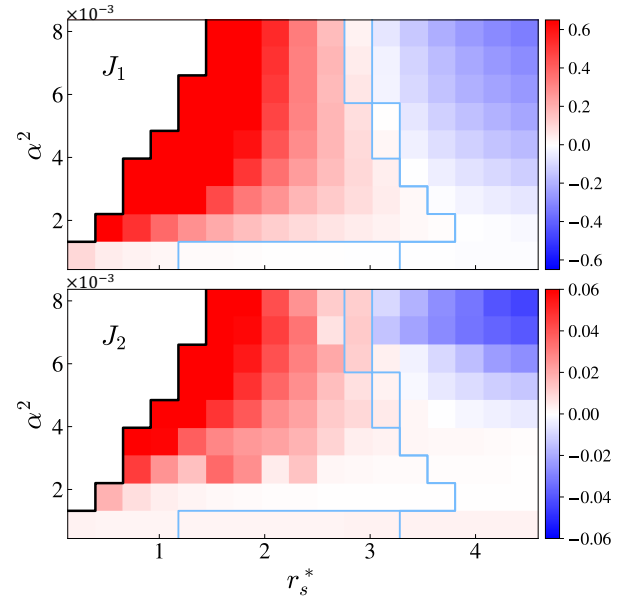


FIG. 5. Values of J_1 and J_2 in units of meV for a fixed a_M throughout the phase diagram, obtained by fitting ground state energies of different insulating magnetic order to a J_1 - J_2 Heisenberg model. (See Eq. (17)-(18).) We observe that J_1 changes sign at the antiferromagnet-ferromagnet phase boundary, while J_2 changes sign inside the region of ferromagnetic states.

lowers energies by increasing separations between electrons. In the language of the honeycomb lattice Hubbard model, occupying only one honeycomb sublattice avoids the near-neighbor electron-electron interaction term in the Hamiltonian with coupling constant U_1 .

From the arguments in Sec. II, we anticipate the physical effect of changing a triangular lattice to a honeycomb lattice is (approximately) equivalent to increasing the effective Wannier function width α . For this reason we expect the metal-insulator phase boundary to move towards larger r_s^* as $\phi \rightarrow 60^\circ$, while the antiferromagnet-ferromagnet transition boundary moves towards smaller r_s^* . For a $r_s^* - \alpha^2$ point on the insulating side of the metal-insulator phase boundary, we show in Fig. 6(a), that the lowest energy state changes from a noncollinear magnetic insulator to a 120° semimetallic SDW, and finally to a paramagnetic metal as $\phi \rightarrow 60^\circ$. In contrast, in Fig. 6(b), no phase transition is observed. The ferromagnetic ground state becomes more and more stable as the antiferromagnet-ferromagnet phase boundary moves away towards smaller r_s^* .

Last but not least, we examine the possibility of non-trivial band topology in the magnetically ordered states. For ferromagnetic and stripe states, it's straightforward to show that the spin-projected orbital Hamiltonians are time-reversal invariant. These states therefore cannot have non-zero Chern numbers. The 120° non-collinear states also cannot be topological, since they can be continuously tuned, via intermediate umbrella states, to fer-

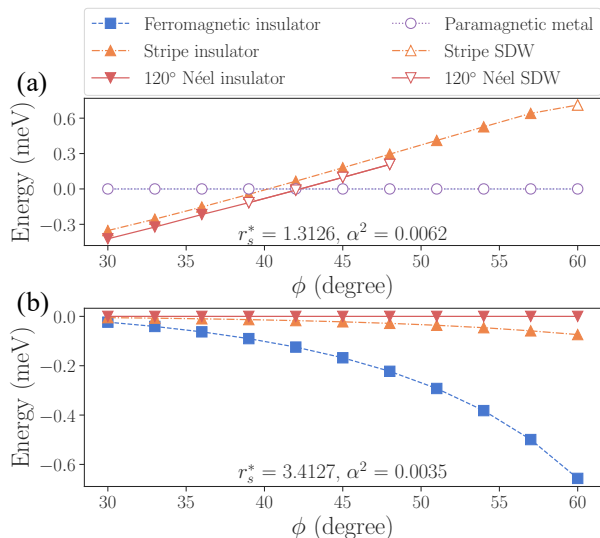


FIG. 6. The parameters (r_s^*, α^2) are chosen to be close to (a) the metal-insulator transition and (b) the antiferromagnet-ferromagnet transition at $\phi = 26^\circ$. We change ϕ from 30° (triangular lattice) to 60° (honeycomb lattice). (a) Energy density is plotted relative to the paramagnetic states. An insulator-to-metal transition is observed as we increase ϕ . (b) Energy density is plotted relative to 120° Néel insulators. We don't see any phase transitions in this case.

romagnetic states without closing the gap between occupied and empty states. More generally any magnetic insulator that is close to a classical spin state with specific spin-orientations on specific sites cannot have a total band Chern number that is non-zero, even if not co-planar. The quantum anomalous Hall effect requires itinerancy in this sense. The absence of non-trivial band topology is consistent with the approach used to approximate the phase boundary analytically. since only in this case are the Wannier functions exponentially localized allowing a Gaussian be a good approximation.

Next we make a stronger claim, namely that the intrinsic anomalous Hall conductance is required to be zero even at finite doping whenever the magnetic state is co-planar. One feature of the heterobilayer continuum Hamiltonian, the lack of inversion symmetry, except at honeycomb values of ϕ , can lead to ground states with non-zero momentum-space Berry curvature $\Omega(\mathbf{k})$ [45]. In the 120° Néel state, for example [46]. Because the TRS-breaking 120° state has $\mathcal{T}' \equiv \mathcal{T} \exp(i\pi \mathbf{S}^\perp)$ symmetry, where \mathbf{S}^\perp is the spin operator perpendicular to the 120° ordering plane, it follows that $\Omega(\mathbf{k}) = -\Omega(-\mathbf{k})$ and that the topological Chern index obtained by integrating the Berry curvature over the Brillouin-zone vanishes. It's worth noting that this new composite anti-unitary symmetry \mathcal{T}' squares to +1, hence does not imply Kramers degeneracy. (See Fig. 2 for band structures.) Therefore \mathcal{T}' is an effective spinless TRS, ensuring that the band structure satisfies $E_n(k) = E_n(-k)$. This gives the stronger constraint that anomalous Hall conductivity is

zero for all doped system.

While it's certainly possible to measure this non-zero Berry curvature through a non-linear Hall effect [47], it's hard to distinguish the ferromagnetic and the 120° order, since both share the same qualitative Berry curvature properties. We propose an alternate strategy to identify the 120° state that exploits the proximity of non-collinear umbrella [48] states in which all spins are tilted toward the direction of an applied magnetic field, breaking \mathcal{T}' . Unlike collinear states, coplanar states can evolve into non-coplanar states under a Zeeman field \mathbf{B} . \mathcal{T}' symmetry can only be broken by a non-coplanar magnetic structure. It's known, however, coplanar configurations are always favored by quantum fluctuations in a isotropic Heisenberg triangular lattice model system under a Zeeman field [49, 50]. Our proposal therefore relies on anisotropies present in more realistic continuum model beyond the simplest approximation taken by Eq. (2). If the anisotropy is not strong enough to realize the non-coplanar state, the 120° coplanar state can also be measured by its distinctive field dependent magnetization curve $\mathbf{M}(\mathbf{B})$. Quantum fluctuations favors the collinear UUD state, among the many competitive coplanar states [49], at a \mathbf{B} -field of around one-third the saturation value, where $\mathbf{M}(\mathbf{B})$ shows a wide plateau [48]. These properties motivate future studies aimed at achieving a full understanding of magnetic anisotropies in triangular lattice TMD moiré materials.

IV. DISCUSSION AND OUTLOOK

In this paper we have examined the phase diagram of moiré Hubbard model systems for the special case of half-filling of the lowest energy band. At this filling factor interaction-induced insulating states are normally identified as Mott insulators. The moiré band Hamiltonian [1] depends on a semiconductor effective mass m^* , the moiré potential modulation strength V_M , the moiré lattice constant a_M , and in addition on a moiré potential shape parameter ϕ that interpolates between triangular and honeycomb lattice cases. The interaction term is sensitive to screening by polarizable backgrounds (including but not necessarily limited to [51] screening by the surrounding dielectric), which we characterize collectively by an effective inverse dielectric constant ϵ^{-1} . At fixed band filling, the model parameters can be collapsed to the shape parameter ϕ and two dimensionless coupling constant ratios, r_s^* and α^2 , chosen with the goal of minimizing the dependence of the phase diagram on ϕ . r_s^* is the standard electron gas density parameter and α^2 is proportional to the fraction of the unit cell area occupied by the model's Wannier orbital. We find a phase diagrams with two prominent transitions, an expected Mott transition between metallic and insulating states, and an unexpected transition between antiferromagnetic and ferromagnetic insulating states. We predict that the metal-insulator transition occurs along a line of nearly

constant $U/t_1 \sim 15.1$, where U is the on-site Hubbard interaction and t_1 is the triangular lattice near-neighbor hopping parameter. The value of this ratio on the metal-insulator transition line is comparable to values obtained in numerical studies of simple on-site-interaction triangular lattice Hubbard models [52, 53].

The metal-insulator transition line can be crossed by changing the electron density parameter r_s^* by changing twist angle, by engineering the depth of the modulating moiré potential via suitable choice of materials, or *in situ* by tuning gate voltages [23, 24] or applying pressure [7]. On the insulating side of the metal-insulator transition we find the 120° three-sublattice antiferromagnet expected on triangular lattices with antiferromagnetic interactions between spins. Within the Hartree-Fock approximation, we find a narrow band of intermediate semimetallic states that maintain the 120° semimetallic SDW order of the insulating state. The phase transition between the SDW state and the strongly metallic state is first order.

The SDW phase that appears in our calculations provides one possible explanation for the complex crossover between insulating and metallic states seen in recent experiments [23, 24], which hint at an intermediate state with a small but finite zero-temperature conductivity [54].

In closing we comment that in this MS we focused on the simplest case in which electronic states are formed from a single microscopic band, and therefore described in a continuum model by two-component spinors. In the case of TMD homobilayers [55–58], and in the case of heterobilayers modified by suitable large gate electric fields [59], low-energy bands are present in both layers, yielding low-energy models with four component spinors that capture both spin and layer degrees of freedom and opening up new opportunities to establish topologically non-trivial states. Indeed recent heterobilayer experiments [25] find transitions to states with spontaneous valley polarization and anomalous Hall effects in TMDs. We have also limited our attention to one electron per moiré period. Doping way from this limit, enriches the physics even more and is thought to lead to superconductivity in some cases. Finally, we have neglected disorder, which might be relevant experimentally, as suggested by the temperature-dependent resistances measured in Ref. [23], which exhibit bumps on the metallic side of the metal-insulator transition similar to the ones seen in Si-MOSFETs [60]. The situation studied in this MS is explores only one simplest limit of the rich physics that remains to be explored in TMD moiré materials.

ACKNOWLEDGMENTS

We acknowledge helpful discussions with Nicolás Morales-Durán, Pawel Potasz, Ajesh Kumar and Jihang Zhu. This work was supported by the U.S. Department of Energy, Office of Science, Basic Energy Sciences, un-

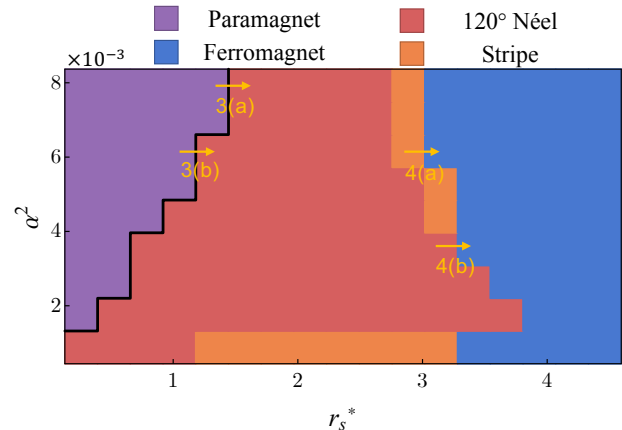


FIG. 7. Pixelated phase diagram for triangular lattice ($\phi = 26^\circ$) moiré materials within Hartree-Fock approximation.

der Award DE-FG02-02ER45958. The authors acknowledge the Texas Advanced Computing Center (TACC) at The University of Texas at Austin for providing HPC resources that have contributed to the research results reported within this paper.

Appendix A: More details on the self-consistent Hartree-Fock calculations

To make the continuum model feasible for a numerical calculation, it's necessary to impose both upper- and lower-cutoffs in the momentum space. In the atomic-insulator limit, the real-space Wannier function is well approximated by Gaussian in a harmonic potential, as argued in the main text. It's then clear that the relevant scale for the upper-cutoff can be obtained by comparing the momentum-space Wannier function width with the moiré Brillouin zone size:

$$\frac{1}{a_W} / |\vec{b}| = \sqrt{\frac{m^* \omega}{\hbar}} / |\vec{b}| = \frac{\sqrt{3}}{4\pi} \left(\frac{\beta m^* V_M}{\hbar^2} \right)^{1/4} \sqrt{a_M}. \quad (\text{A1})$$

That is to say a larger upper-cutoff may be required for stronger interactions. The resulting dimensionless number is of $\mathcal{O}(1)$ in our calculation, and we keep the number of momentum shells in the continuum model such that more shells don't change the Hartree-Fock energies up to the convergence accuracy.

As for the lower-cutoff, we note that energy density for a periodic system with Coulomb interactions suffers from a finite-size correction, which depends not only on the total number of mesh points N in the moiré Brillouin zone but also on the geometrical detail of the mesh. We correct the finite-size effect by choosing the geometry such that it's compatible with all the pertinent magnetic moiré Brillouin zones, and meshing the moiré Brillouin zone always in the same way. In other words, we hold

the real-space sample size N fixed for all calculations, which is 108 in our phase diagram calculations. Since the leading finite-size corrections to energy are now state independent, they can be eliminated by evaluating energy differences between states at fixed system size. We do not actually extrapolate the energies toward the thermodynamic limit since the extrapolation itself incurs further uncertainty.

The actual phase diagram from the self-consistent Hartree-Fock calculation is shown in Fig. 7. Fig. 1 in the main text is obtained by fitting the analytical form of the phase boundary to Fig. 7. In the limit of $\alpha \rightarrow 0$, we observe different spin configurations converge to the same energy due to the vanishing of the exchange energies J , which we do not show in the main text.

To show the Hartree-Fock band structures in Fig. 2(b) with a clear small Fermi surface, we increase the system size N to 432. A caveat here is that when we consider a specific magnetic ordered insulating state, the gap size

is dependent on the system size because the interaction $U \propto -1/\sqrt{N}$. Hence there is a slight mismatch in parameters and phases between Fig. 2 and 3. This finite-size correction to the gap size is small when N is large, so the phase boundary of the 120° semimetallic SDW state is still relatively accurate in Fig. 1.

Appendix B: Perturbative effects of “nonlocal” interactions

In this section, we illustrate the induced spin-spin interactions by V_{ah} and V_x in the presence of a large- U Hubbard interaction. For simplicity, we always consider the half-filled case and zero-hopping limit. The ground state lies in the no doubly-occupied site sector as in a usual Hubbard model. It can be readily seen that V_{ah} perturbs the ground state out of this sector, so the lowest order contribution is of order $\mathcal{O}(|V_{ah}|^2/U)$. In spirit of the t/U expansion [41], the leading order terms are

$$-U^{-1} \sum_{\sigma_1, \sigma_2} \left[\langle 2\sigma_2, 1\bar{\sigma}_2 | V_C | 1\sigma_2, 1\bar{\sigma}_2 \rangle \langle 1\sigma_1, 1\bar{\sigma}_1 | V_C | 1\sigma_1, 2\bar{\sigma}_1 \rangle c_{2\sigma_2}^\dagger c_{1\bar{\sigma}_2}^\dagger c_{1\sigma_2} c_{1\sigma_1} c_{1\bar{\sigma}_1}^\dagger c_{2\bar{\sigma}_1}^\dagger c_{1\sigma_1} + \right. \\ \left. \langle 1\sigma_2, 2\bar{\sigma}_2 | V_C | 1\sigma_2, 1\bar{\sigma}_2 \rangle \langle 1\sigma_1, 1\bar{\sigma}_1 | V_C | 1\sigma_1, 2\bar{\sigma}_1 \rangle c_{1\sigma_2}^\dagger c_{2\bar{\sigma}_2}^\dagger c_{1\bar{\sigma}_2} c_{1\sigma_2} c_{1\sigma_1}^\dagger c_{1\bar{\sigma}_1}^\dagger c_{2\bar{\sigma}_1} c_{1\sigma_1} \right] + h.c., \quad (\text{B1})$$

where 1 and 2 label nearest neighbors. The fermionic interactions of the two terms in the square brackets are actually related by a relabeling symmetry: the second term ($\sigma_2 \rightarrow \bar{\sigma}_2$) = the first term. The first term in Eq. (B1) can be simplified, using $\sum_\sigma n_{i\sigma} = 1$, to $-|V_{ah}|^2 U^{-1} \left(-\sum_\sigma c_{1\sigma}^\dagger c_{1\bar{\sigma}}^\dagger c_{2\bar{\sigma}}^\dagger c_{2\sigma} + \sum_\sigma n_{1\sigma} n_{2\bar{\sigma}} \right) = -|V_{ah}|^2 U^{-1} (1 - \boldsymbol{\sigma}_1 \cdot \boldsymbol{\sigma}_2) / 2$, where $\sigma_i = c_{i\alpha}^\dagger \sigma_{\alpha\beta} c_{i\beta}$ and $|V_{ah}|^2 = \langle 2, 1 | V_C | 1, 1 \rangle \langle 1, 1 | V_C | 1, 2 \rangle$. Hence it gives rise to the same type of contribution as the normal hopping term in Hubbard model, i.e. antiferromagnetic coupling.

Now we turn to consider the effects of V_x . V_x actually

leaves the number of doubly occupied sites invariant. So the lowest order contribution is just itself:

$$\sum_{\sigma_1, \sigma_2} \langle 2\sigma_1, 1\sigma_2 | V_C | 1\sigma_1, 2\sigma_2 \rangle c_{2\sigma_1}^\dagger c_{1\sigma_2}^\dagger c_{2\sigma_2} c_{1\sigma_1} \quad (\text{B2})$$

$$= \langle 2, 1 | V_C | 1, 2 \rangle \sum_{\sigma_1, \sigma_2} c_{2\sigma_1}^\dagger c_{1\sigma_2}^\dagger c_{2\sigma_2} c_{1\sigma_1} \quad (\text{B3})$$

$$= -\frac{\langle 2, 1 | V_C | 1, 2 \rangle}{2} (1 + \boldsymbol{\sigma}_1 \cdot \boldsymbol{\sigma}_2), \quad (\text{B4})$$

which favors ferromagnetic spin configuration.

-
- [1] F. Wu, T. Lovorn, E. Tutuc, and A. H. MacDonald, Hubbard model physics in transition metal dichalcogenide moiré bands, *Phys. Rev. Lett.* **121**, 026402 (2018).
- [2] R. Bistritzer and A. H. MacDonald, Moiré bands in twisted double-layer graphene, *Proceedings of the National Academy of Sciences* **108**, 12233 (2011).
- [3] E. Suárez Morell, J. D. Correa, P. Vargas, M. Pacheco, and Z. Barticevic, Flat bands in slightly twisted bilayer graphene: Tight-binding calculations, *Phys. Rev. B* **82**, 121407 (2010).
- [4] K. Kim, A. DaSilva, S. Huang, B. Fallahzad, S. Larentis, T. Taniguchi, K. Watanabe, B. J. LeRoy, A. H. MacDonald, and E. Tutuc, Tunable moiré bands and strong correlations in small-twist-angle bilayer graphene, *Proceedings of the National Academy of Sciences* **114**, 3364 (2017).
- [5] Y. Cao, V. Fatemi, A. Demir, S. Fang, S. L. Tomarken, J. Y. Luo, J. D. Sanchez-Yamagishi, K. Watanabe, T. Taniguchi, E. Kaxiras, *et al.*, Correlated insulator behaviour at half-filling in magic-angle graphene superlattices, *Nature* **556**, 80 (2018).
- [6] Y. Cao, V. Fatemi, S. Fang, K. Watanabe, T. Taniguchi, E. Kaxiras, and P. Jarillo-Herrero, Unconventional superconductivity in magic-angle graphene superlattices, *Nature* **556**, 43 (2018).
- [7] M. Yankowitz, S. Chen, H. Polshyn, Y. Zhang, K. Watan-

- abe, T. Taniguchi, D. Graf, A. F. Young, and C. R. Dean, Tuning superconductivity in twisted bilayer graphene, *Science* **363**, 1059 (2019).
- [8] X. Lu, P. Stepanov, W. Yang, M. Xie, M. A. Aamir, I. Das, C. Urgell, K. Watanabe, T. Taniguchi, G. Zhang, *et al.*, Superconductors, orbital magnets and correlated states in magic-angle bilayer graphene, *Nature* **574**, 653 (2019).
- [9] A. L. Sharpe, E. J. Fox, A. W. Barnard, J. Finney, K. Watanabe, T. Taniguchi, M. Kastner, and D. Goldhaber-Gordon, Emergent ferromagnetism near three-quarters filling in twisted bilayer graphene, *Science* **365**, 605 (2019).
- [10] M. Serlin, C. Tschirhart, H. Polshyn, Y. Zhang, J. Zhu, K. Watanabe, T. Taniguchi, L. Balents, and A. F. Young, Intrinsic quantized anomalous hall effect in a moiré heterostructure, *Science* **367**, 900 (2020).
- [11] Y. Cao, D. Rodan-Legrain, O. Rubies-Bigorda, J. M. Park, K. Watanabe, T. Taniguchi, and P. Jarillo-Herrero, Tunable correlated states and spin-polarized phases in twisted bilayer–bilayer graphene, *Nature*, 1 (2020).
- [12] C. Shen, Y. Chu, Q. Wu, N. Li, S. Wang, Y. Zhao, J. Tang, J. Liu, J. Tian, K. Watanabe, *et al.*, Correlated states in twisted double bilayer graphene, *Nature Physics* **16**, 520 (2020).
- [13] G. Chen, L. Jiang, S. Wu, B. Lyu, H. Li, B. L. Chittari, K. Watanabe, T. Taniguchi, Z. Shi, J. Jung, *et al.*, Evidence of a gate-tunable mott insulator in a trilayer graphene moiré superlattice, *Nature Physics* **15**, 237 (2019).
- [14] G. Chen, A. L. Sharpe, P. Gallagher, I. T. Rosen, E. J. Fox, L. Jiang, B. Lyu, H. Li, K. Watanabe, T. Taniguchi, *et al.*, Signatures of tunable superconductivity in a trilayer graphene moiré superlattice, *Nature* **572**, 215 (2019).
- [15] Y. Tang, L. Li, T. Li, Y. Xu, S. Liu, K. Barmak, K. Watanabe, T. Taniguchi, A. H. MacDonald, J. Shan, *et al.*, Simulation of hubbard model physics in wse 2/ws 2 moiré superlattices, *Nature* **579**, 353 (2020).
- [16] E. C. Regan, D. Wang, C. Jin, M. I. B. Utama, B. Gao, X. Wei, S. Zhao, W. Zhao, Z. Zhang, K. Yumigeta, *et al.*, Mott and generalized wigner crystal states in wse 2/ws 2 moiré superlattices, *Nature* **579**, 359 (2020).
- [17] L. Wang, E.-M. Shih, A. Ghiotto, L. Xian, D. A. Rhodes, C. Tan, M. Claassen, D. M. Kennes, Y. Bai, B. Kim, *et al.*, Correlated electronic phases in twisted bilayer transition metal dichalcogenides, *Nature materials*, 1 (2020).
- [18] Y. Xu, S. Liu, D. A. Rhodes, K. Watanabe, T. Taniguchi, J. Hone, V. Elser, K. F. Mak, and J. Shan, Correlated insulating states at fractional fillings of moiré superlattices, *Nature* **587**, 214 (2020).
- [19] C. Jin, Z. Tao, T. Li, Y. Xu, Y. Tang, J. Zhu, S. Liu, K. Watanabe, T. Taniguchi, J. C. Hone, *et al.*, Stripe phases in wse 2/ws 2 moiré superlattices, *Nature Materials*, 1 (2021).
- [20] T. Li, J. Zhu, Y. Tang, K. Watanabe, T. Taniguchi, V. Elser, J. Shan, and K. F. Mak, Charge-order-enhanced capacitance in semiconductor moiré superlattices, arXiv preprint arXiv:2102.10823 (2021).
- [21] H. Li, S. Li, M. H. Naik, J. Xie, X. Li, E. Regan, D. Wang, W. Zhao, K. Yumigeta, M. Blei, *et al.*, Imaging local discharge cascades for correlated electrons in ws2/wse2 moiré superlattices, arXiv preprint arXiv:2102.09986 (2021).
- [22] X. Huang, T. Wang, S. Miao, C. Wang, Z. Li, Z. Lian, T. Taniguchi, K. Watanabe, S. Okamoto, D. Xiao, *et al.*, Correlated insulating states at fractional fillings of the ws2/wse2 moiré lattice, *Nature Physics* **17**, 715 (2021).
- [23] T. Li, S. Jiang, L. Li, Y. Zhang, K. Kang, J. Zhu, K. Watanabe, T. Taniguchi, D. Chowdhury, L. Fu, *et al.*, Continuous mott transition in semiconductor moiré superlattices, arXiv preprint arXiv:2103.09779 (2021).
- [24] A. Ghiotto, E.-M. Shih, G. S. Pereira, D. A. Rhodes, B. Kim, J. Zang, A. J. Millis, K. Watanabe, T. Taniguchi, J. C. Hone, *et al.*, Quantum criticality in twisted transition metal dichalcogenides, arXiv preprint arXiv:2103.09796 (2021).
- [25] T. Li, S. Jiang, B. Shen, Y. Zhang, L. Li, T. Devakul, K. Watanabe, T. Taniguchi, L. Fu, J. Shan, *et al.*, Quantum anomalous hall effect from intertwined moiré bands, arXiv preprint arXiv:2107.01796 (2021).
- [26] M. Angeli and A. H. MacDonald, γ valley transition metal dichalcogenide moiré bands, *Proceedings of the National Academy of Sciences* **118** (2021).
- [27] Y. Zhang, N. F. Q. Yuan, and L. Fu, Moiré quantum chemistry: Charge transfer in transition metal dichalcogenide superlattices, *Phys. Rev. B* **102**, 201115 (2020).
- [28] J. P. Perdew and A. Zunger, Self-interaction correction to density-functional approximations for many-electron systems, *Phys. Rev. B* **23**, 5048 (1981).
- [29] N. Morales-Durán, A. H. MacDonald, and P. Potasz, Metal-insulator transition in transition metal dichalcogenide heterobilayer moiré superlattices, *Phys. Rev. B* **103**, L241110 (2021).
- [30] T. Jolicoeur, E. Dagotto, E. Gagliano, and S. Bacci, Ground-state properties of the $s=1/2$ heisenberg antiferromagnet on a triangular lattice, *Phys. Rev. B* **42**, 4800 (1990).
- [31] F. Wu, T. Lovorn, and A. H. MacDonald, Topological exciton bands in moiré heterojunctions, *Phys. Rev. Lett.* **118**, 147401 (2017).
- [32] This choice of β assures that the harmonic expansion is performed around the global minimum of the modulation potential. The properties of TMD moiré materials are invariant under $\phi \rightarrow -\phi$, and $\phi \rightarrow \phi + k120^\circ$.
- [33] Tanatar and Ceperley, Ground state of the two-dimensional electron gas., *Physical review. B, Condensed matter* **39** **8**, 5005 (1989).
- [34] C. Attaccalite, S. Moroni, P. Gori-Giorgi, and G. Bachelet, Correlation energy and spin polarization in the 2d electron gas., *Physical review letters* **88** **25 Pt 1**, 256601 (2002).
- [35] R. Kaneko, S. Morita, and M. Imada, Gapless spin-liquid phase in an extended spin 1/2 triangular heisenberg model, *Journal of the Physical Society of Japan* **83**, 093707 (2014).
- [36] Z. Zhu and S. R. White, Spin liquid phase of the $s = \frac{1}{2} J_1 - J_2$ heisenberg model on the triangular lattice, *Phys. Rev. B* **92**, 041105 (2015).
- [37] W.-J. Hu, S.-S. Gong, W. Zhu, and D. N. Sheng, Competing spin-liquid states in the spin- $\frac{1}{2}$ heisenberg model on the triangular lattice, *Phys. Rev. B* **92**, 140403 (2015).
- [38] Y. Iqbal, W.-J. Hu, R. Thomale, D. Poilblanc, and F. Becca, Spin liquid nature in the heisenberg $J_1 - J_2$ triangular antiferromagnet, *Phys. Rev. B* **93**, 144411 (2016).
- [39] S.-S. Gong, W. Zhu, J.-X. Zhu, D. N. Sheng, and

- K. Yang, Global phase diagram and quantum spin liquids in a spin- $\frac{1}{2}$ triangular antiferromagnet, *Phys. Rev. B* **96**, 075116 (2017).
- [40] Z. Zhu, P. A. Maksimov, S. R. White, and A. L. Chernyshev, Topography of spin liquids on a triangular lattice, *Phys. Rev. Lett.* **120**, 207203 (2018).
- [41] A. H. MacDonald, S. M. Girvin, and D. Yoshioka, $\frac{t}{U}$ expansion for the hubbard model, *Phys. Rev. B* **37**, 9753 (1988).
- [42] See also N. Morales-Durán, N. C. Hu, P. Potasz, and A. H. MacDonald, Relevance of non-local interactions in moiré Hubbard systems, in preparation.
- [43] See Appendix B for a more formal explanation via an expansion around the flat-band limit.
- [44] Increasing α^2 , the parameter that measures the relative spread of the Wannier functions, increases both t_1 and $|V_x|$. From Eq. (13) and (21) we see that $|V_x|$ increases more rapidly than t_1^2 . This explains why $\alpha^2 \sim 1/r_s^*$ along the ferromagnetic/antiferromagnetic phase boundary.
- [45] D. Xiao, M.-C. Chang, and Q. Niu, Berry phase effects on electronic properties, *Rev. Mod. Phys.* **82**, 1959 (2010).
- [46] H. Chen, Q. Niu, and A. H. MacDonald, Anomalous hall effect arising from noncollinear antiferromagnetism, *Phys. Rev. Lett.* **112**, 017205 (2014).
- [47] I. Sodemann and L. Fu, Quantum nonlinear hall effect induced by berry curvature dipole in time-reversal invariant materials, *Phys. Rev. Lett.* **115**, 216806 (2015).
- [48] O. A. Starykh, Unusual ordered phases of highly frustrated magnets: a review, *Reports on Progress in Physics* **78**, 052502 (2015).
- [49] M. Ye and A. V. Chubukov, Quantum phase transitions in the heisenberg $J_1 - J_2$ triangular antiferromagnet in a magnetic field, *Phys. Rev. B* **95**, 014425 (2017).
- [50] D. Farnell, R. Bishop, and J. Richter, Non-coplanar model states in quantum magnetism applications of the high-order coupled cluster method, *Journal of Statistical Physics* **176**, 180 (2019).
- [51] X. Liu, Z. Wang, K. Watanabe, T. Taniguchi, O. Vafek, and J. Li, Tuning electron correlation in magic-angle twisted bilayer graphene using coulomb screening, *Science* **371**, 1261 (2021).
- [52] A. Szasz, J. Motruk, M. P. Zaletel, and J. E. Moore, Chiral spin liquid phase of the triangular lattice hubbard model: A density matrix renormalization group study, *Phys. Rev. X* **10**, 021042 (2020).
- [53] L. F. Tocchio, A. Montorsi, and F. Becca, Magnetic and spin-liquid phases in the frustrated $t - t'$ hubbard model on the triangular lattice, *Phys. Rev. B* **102**, 115150 (2020).
- [54] A resistance jump also occurs at the critical point in electron-fractionalization [61, 62] metal-insulator transition scenarios, but for completely different reasons.
- [55] F. Wu, T. Lovorn, E. Tutuc, I. Martin, and A. H. MacDonald, Topological insulators in twisted transition metal dichalcogenide homobilayers, *Phys. Rev. Lett.* **122**, 086402 (2019).
- [56] H. Pan, F. Wu, and S. Das Sarma, Band topology, hubbard model, heisenberg model, and dzyaloshinskii-moriya interaction in twisted bilayer wse₂, *Phys. Rev. Research* **2**, 033087 (2020).
- [57] J. Zang, J. Wang, J. Cano, and A. J. Millis, Hartree-fock study of the moiré hubbard model for twisted bilayer transition metal dichalcogenides, arXiv preprint arXiv:2105.11883 (2021).
- [58] T. Devakul, V. Crépel, Y. Zhang, and L. Fu, Magic in twisted transition metal dichalcogenide bilayers, arXiv preprint arXiv:2106.11954 (2021).
- [59] Y. Zhang, T. Devakul, and L. Fu, Spin-textured chern bands in ab-stacked transition metal dichalcogenide bilayers, arXiv preprint arXiv:2107.02167 (2021).
- [60] A. Punnoose and A. M. Finkel'stein, Dilute electron gas near the metal-insulator transition: Role of valleys in silicon inversion layers, *Phys. Rev. Lett.* **88**, 016802 (2001).
- [61] T. Senthil, Theory of a continuous mott transition in two dimensions, *Phys. Rev. B* **78**, 045109 (2008).
- [62] Y. Xu, Z.-X. Luo, C.-M. Jian, and C. Xu, Metal-insulator transition with charge fractionalization, arXiv preprint arXiv:2106.14910 (2021).